Research Article

Exploring the First High-Entropy Thin Film Libraries: Composition Spread-Controlled Crystalline Structure

Thi Xuyen Nguyen, Yen-Hsun Su, Jason Hattrick-Simpers, Howie Joress, Takahiro Nagata, Kao-Shuo Chang, Suchismita Sarker, Apurva Mehta, and Jyh-Ming Ting*

Read Online

ACCESS | Metrics & More | Article Recommendations | Supporting Information

ABSTRACT: Thin films of two types of high-entropy oxides (HEOs) have been deposited on 76.2 mm Si wafers using combinatorial sputter deposition. In one type of the oxides, $(MgZnMnCoNi)O_x$ all the metals have a stable divalent oxidation state and similar cationic radii. In the second type of oxides, $(CrFeMnCoNi)O_x$, the metals are more diverse in the atomic radius and valence state, and have good solubility in their sub-binary and ternary oxide systems. The resulting HEO thin films were characterized using several high-throughput analytical techniques. The microstructure, composition, and electrical conductivity obtained on defined grid maps were obtained for the first time across large compositional ranges. The crystalline structure of the films was observed as a function of the metallic elements in the composition spreads, that is, the Mn and Zn in $(MgZnMnCoNi)O_x$ and Mn and Ni in $(CrFeMnCoNi)O_x$. The $(MgZnMnCoNi)O_x$ sample was observed to form two-phase structures, except single spinel structure was found in $(MgZnMnCoNi)O_x$ over a range of Mn > 12 at. % and Zn < 44 at. %, while $(CrFeMnCoNi)O_x$ was always observed to form two-phase structures. Composition-controlled crystalline structure is not only experimentally demonstrated but also supported by density function theory calculation.

KEYWORDS: high-entropy oxide, combinatorial sputter deposition, high-throughput analysis, composition-controlled crystalline structure
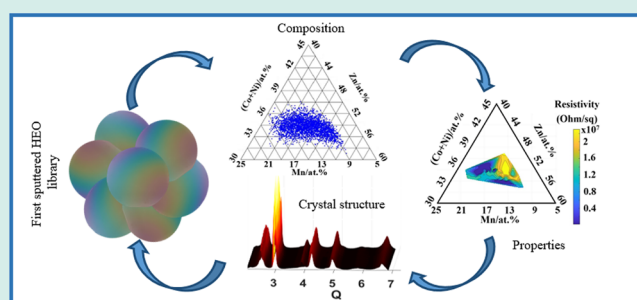
INTRODUCTION

The first demonstration of high-entropy alloy (HEA) in 2004[1,2] has led to intensive investigations on various classes of nonmetallic high-entropy materials, such as high-entropy oxides (HEOs),[3−7] carbides,[8−11] diborides,[12,13] nitrides,[14,15] silicides,[16,17] and chalcogenides,[18] because of their expected multifunctional properties. These nonmetallic high-entropy materials are fundamentally different from HEAs; hence, their properties and potential applications are different too.[19−21] Because of the complexity of studying HEOs, to date, there have been relatively few studies investigating the vast number of compositions and morphologies of potential HEOs. Currently, HEOs can be divided into two groups based on the elements involved: transition metal-based oxides and rare earth metal-based HEOs.

The transition metal-based (MgCoNiCuZn)O system is by far the most studied HEO class.[3,22−24] Equimolar (MgCoNiCuZn)O exhibiting a single-phase rock salt structure was pioneered by Rost et al. in 2015.[3] (MgCoNiCuZn)O was synthesized using a solid-state reaction process in which the constituent oxides were used as the starting materials. This was the first demonstration that entropy could dominate the free energy in oxides stabilizing a crystalline oxide having five metal cations. Following this publication, (MgCoNiCuZn)O-based

HEO powders and films[25,26] were reported. The resulting crystalline structures were reported to be mostly rock salt structures that had unique and promising properties and excellent performance. (MgCoNiCuZn)O powders are of interest for their physical properties (e.g., dielectric constant[27] and magnetic properties[23]) and applications.[28−31] On the other hand, thin-film (MgCoNiCuZn)O-based HEOs are much less explored except a few studies reporting their thermal stability[26] and antiferromagnetic properties.[25] In addition to the rock salt structure, these compounds have also been observed to form spinel oxides.[32−35]

HEOs represent a new and exciting class of materials to be explored. The huge space for exploration provides the tantalizing opportunity for tuning material properties by understanding and controlling the processing-composition-phase-property relationships of these materials. All of these depend upon the understanding of material characteristics, which begins with and
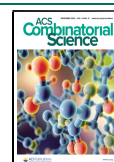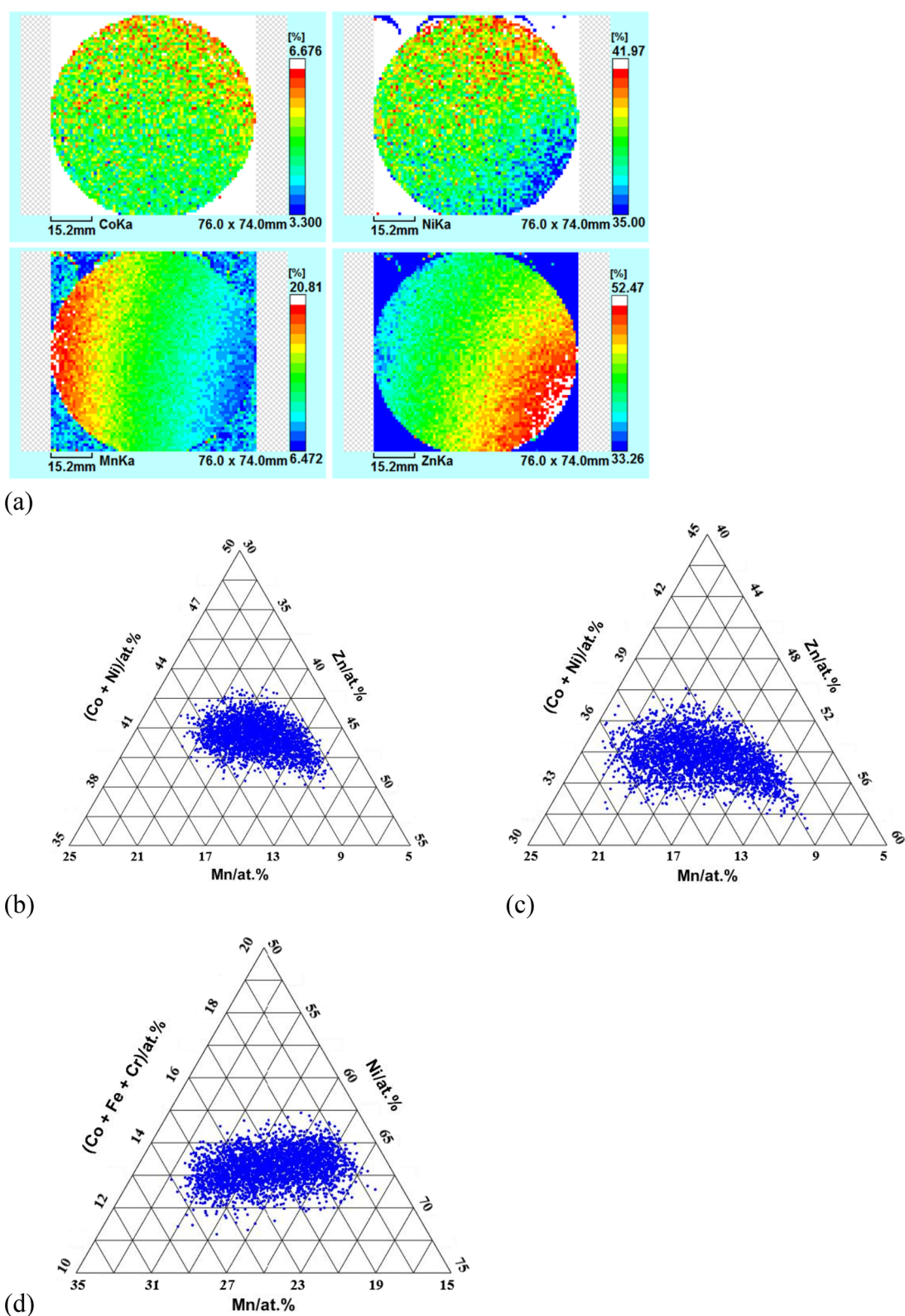
Figure 1. (a) Element contour plots for RS1. Ternary diagrams for (b) RS1, (c) RS2, and (d) SP.

is closely related to the synthesis of the material. Currently, HEO powders or pellets are synthesized through solid-state reactions, wet chemical processes, and thermal pyrolysis; while thin-film HEOs are obtained using pulsed laser deposition.[25,26,36] Typically such studies are performed using traditional one-sample-at-a-time synthesis techniques which restricts the rate of

study, slowing down the pace of HEO research, particularly given the large parameter space. Hence, a rapid synthesis and characterization approach is desired to speed the rate of discovery and eventually deployment. So far, there have been very few studies on HEO thin films that address the compositional dependence of their structural stability and

properties. For low-order complex materials, combinatorial chemistry has been proven to be a powerful tool for exploring the material characteristics.[37−39] It is, therefore, our objective to use combinatorial sputter deposition to make HEO thin films, which are then characterized using several high throughput analytical techniques. The combinatorial sputter deposition technique also permits the systematic study of nonequimolar HEOs, which are key to the tunability of their functional properties.

Here, we present the high-throughput study of two different systems of thin-film HEOs, including $(MgZnMnCoNi)O_x$ and $(CrFeMnCoNi)O_x$ via combinatorial thin-film sputtering with widely varying nonequiatomic compositions. $(MgZnMnCoNi)O_x$ involves five metals of Mg, Zn, Mn, Co, and Ni. $(CrFeMnCoNi)O_x$ involves five metals of Cr, Fe, Mn, Co, and Ni. In the first system, all the metals have stable divalent oxidation state, similar cationic radii, and coordination numbers. The specific divalent oxides, Co, Ni, Mn, Mg, and Zn have a cationic radius of 0.65, 0.69, 0.7, 0.72, and 0.6 nm, respectively.[40] Their sub-binary oxides show good solubility between the two oxides, except that MgO and ZnO have limited solubility in each other. The metals in the second system are more diverse in cationic radii and valence states but still exhibit great solubility in their sub-binary and subternary oxide systems. It is, therefore, believed that the metal oxides would result in a solid solution based on the rule of solubility.[41] These thin-film HEOs have been deposited using combinatorial sputter deposition. We demonstrate that with a total of three common metals (Mn, Co, and Ni) in both systems, the resulting films consist of both rock salt and spinel structures. However, by adjusting the sputter power and replacing the Cr and Fe with Mg and Zn single-phase spinel can be formed. Such compositional-controlled structure is demonstrated experimentally and theoretically.

EXPERIMENTAL SECTION

Combinatorial Synthesis. $(MgZnMnCoNi)O_x$ and $(CrFeMnCoNi)O_x$ thin-film libraries were obtained via combinatorial RF cosputtering of a MnO target (UMAT, 99.9% pure) and (MgCoNiZn) and (CrFeCoNi) composite targets (UMAT, 99.9% pure), respectively, on 76.2 mm [100] Si wafers. The composite target consisted of 4 segmented metal wedges hot pressed to form a single 76.2 mm diameter target. The films were deposited under an Ar/O_2 ratio of 10:1 and at a working pressure of 0.4 Pa (3 mTorr). During deposition, the substrates were heated to a temperature of 800 °C. For the $(MgZnMnCoNi)O_x$ system, two films were grown, RS1 and RS2. For both films, the (MgCoNiZn) target power was 100 W, but the MnO target powers were 100 and 80 W for RS1 and RS2, respectively. The MnO and (CrFeCoNi) target powers for the deposition of $(CrFeMnCoNi)O_x$ thin films were 100 and 80 W, respectively. The $(CrFeMnCoNi)O_x$ sample is designated as SP. After the deposition, the samples were cooled to room temperature under vacuum.

High-Throughput Characterization. The material libraries were investigated by high-throughput characterization techniques. The metal composition was characterized with an X-ray fluorescence spectrometer (XRF, Shimadzu, μEDX-1400). The accelerating voltage of the XRF is 50 kV (Rh target, 100 μA). The whole wafer was mapped with a spot size of 1 mm × 1 mm. Since the XRF cannot detect Mg, we used SEM EDS with accelerating voltage of 10 kV (10 μA) as a supplementary tool to show the existence and distribution of Mg. The concentration of Mg was detected at different positions in the

thin-film wafer. The sheet resistivity was determined using a four-probe scanning system (Napson, RT3000RG-80N) with a spot size of 7 × 7 mm. High-throughput structural characterization was performed at the Stanford Synchrotron Radiation Light Source beamline 1−5. Details regarding the end station and the measurement grid can be found in refs 42 and 43.

Simulation. The formation energy of the HEO was calculated via density function theory (DFT) using VASP6.0 (Vienna Ab initio Simulation Package). The pseudopotential was generated using the projector augmented wave method. The exchange-correlation energy was described by the generalized gradient approximation (GGA) in the parametrization of Perdew−Becke−Ernzehof.[44] The cutoff energy was 520 eV. The gamma-centered grid dimensions were 4 × 4 × 4. Supercell dimensions for the RS1 and RS2 were 11.24 Å× 11.24 Å × 11.24 Å and for SP were 8.49 Å× 8.49 Å× 8.49 Å. There were 64 atoms per unit cell in RS1 and RS2 and 56 atoms in SP. All structures considered have been relaxed using the GGA. Both the atomic position and volume have been optimized.

RESULTS AND DISCUSSION

The XRF elemental compositions of the resulting HEO thin films are first presented. Figure 1a shows the contour plots of elements Mn, Co, Ni, and Zn in the RS1. The measured points are shown in the ternary phase diagram (Figure 1b). Because of its low energy florescence line, Mg was not detectable using the XRF. However, EDX analysis shows little variation in the Mg composition, as shown in Figure S1. Table 1 lists the

Table 1. Element Concentration Ranges in Different Films

	Zn (at.%)	Mn (at.%)	Ni (at.%)	Co (at.%)	Cr (at.%)	Fe (at.%)
RS1	33.3−52.5	6.5−20.8	35−41	3.3−6.7		
RS2	38.2−60.4	5.4−22.2	23.5−35.6	3.7−7.9		
SP		14.3−33.9	53.2−70.8	3.5−10.7	1.4−4.7	2.7−6.4

concentration ranges for Mn, Co, Ni, and Zn. The contour plots and the ternary diagrams for the RS2 film are shown in Figures S2a and 1c, respectively; while concentration ranges are given in Table 1. It is seen that both the Mn and Zn show excellent composition spreads across the RS1 and RS2 films, which are $(MgZnMnCoNi)O_x$. The Mn concentration decreases from the left- to the right-hand sides, while the Zn concentration decreases from the upper-left to the upper-right on the film. Much less compositional variation for Co and Ni was found. This could be due to the lower sputtering yield (especially with respect to Zn) or possibly the 4 quarters design of the target coupled with the target-chamber geometry. For the SP film (Figures S2b and 1d), the concentration ranges are presented in Table 1. In this film, only the Mn and Ni show composition spreads across the film, with Mn and Ni decreasing and increasing, respectively, from the left- to the right-hand sides on the film. The other elements exhibit little compositional variation.
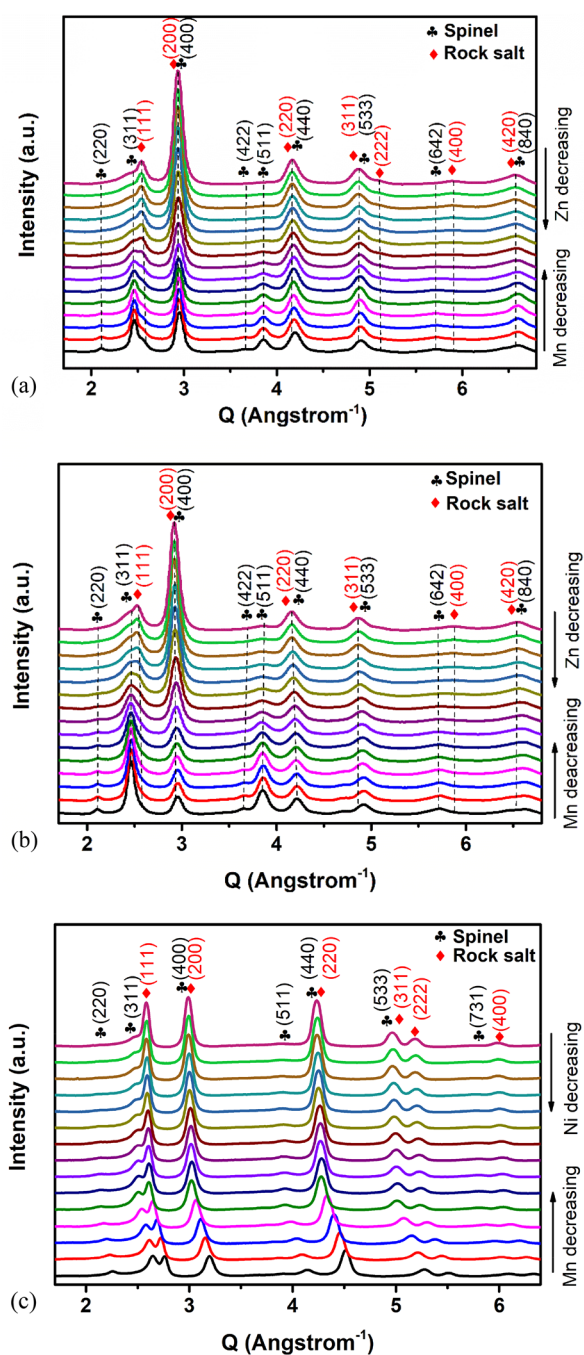
Sheet resistance was determined using a scanning 4-point probe measured on 89 data points of a square grid. The resulting ternary diagrams are shown in Figure 2 for all three films, while sheet resistance contours are displayed in Figure S3. The concentration regions covering the corresponding the 4-point probe measurements are shown in the ternary diagrams. Both
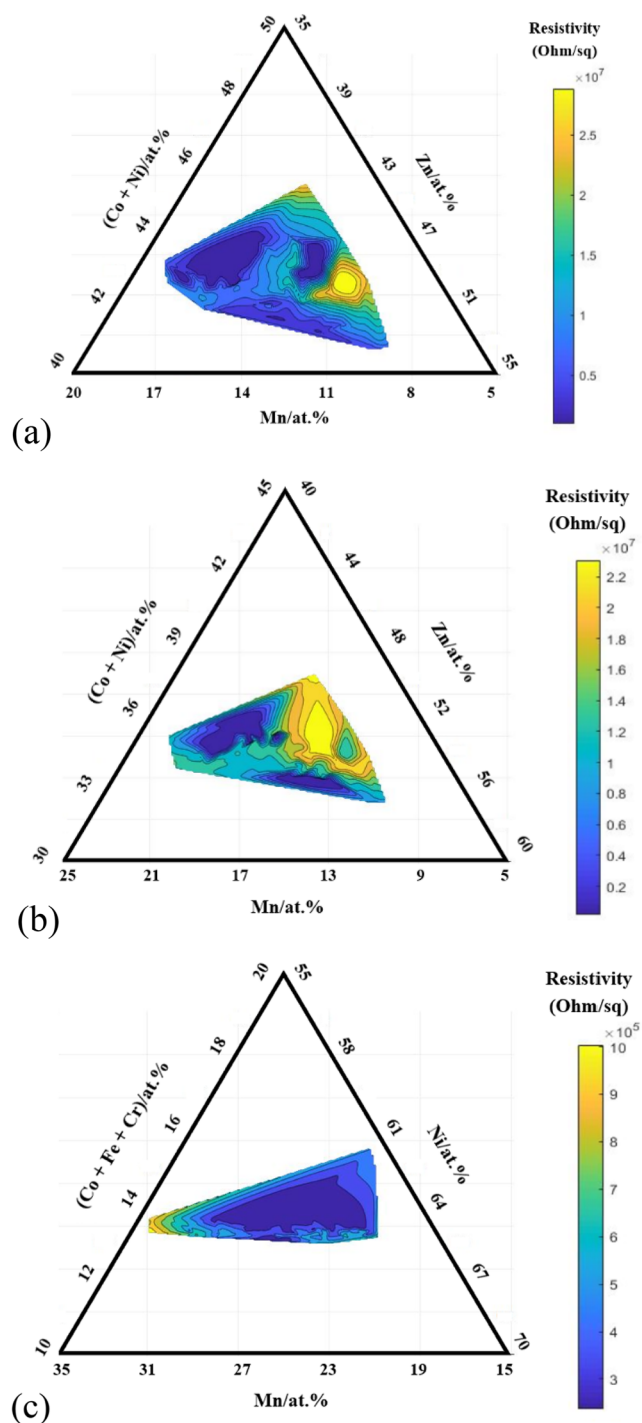
Figure 2. Ternary diagrams of sheet resistance of (a) RS1, (b) RS2, and (c) SP.


Figure 3. XRD patterns across the central horizontal line for (a) RS1, (b) RS2, and (c) SP.

the $(MgZnMnCoNi)O_x$ films (RS1 and RS2) have higher sheet resistance, on the order of 10^6 to 10^7 ohm/sq, compared to the $(CrFeMnCoNi)O_x$ film (SP), which is on the order of 10^5 to 10^6 ohm/sq. It is notable that the sheet resistance continuously decreases with the Mn concentration along the Mn and Zn binary in the RS1 and, much more significantly, in the RS2 films.

Synchrotron XRD scanning was performed to obtain 177 patterns from each of the films; Figure S4a shows the grid positions on the 76.2 mm wafer. The selected XRD patterns across the central horizontal line for all the films are shown in Figure 3a−c; while the top views of all 177 XRD patterns on

each film are shown in Figure S4b−d. Spinel and rock salt structures were found in all three samples. RS1 and RS2, having the same constituent elements, show quite similar XRD diffraction profiles. No wurtzite ZnO phase was observed even with high Zn concentration. There is little peak shift with the Mn and Zn concentration variations. The lattice spacing therefore shows minimal concentration dependence (Figure 4). The lattice spacing was calculated from the spinel (311) diffraction plane and rock salt (111) diffraction plane. However, SP shows significant peak shifts toward to higher diffraction angles in limited concentration ranges, as shown by the lower 4 diffraction patterns. Therefore, as shown in Figure 4, in the Mn and Ni binary, d-spacing decreases with Mn concentration.
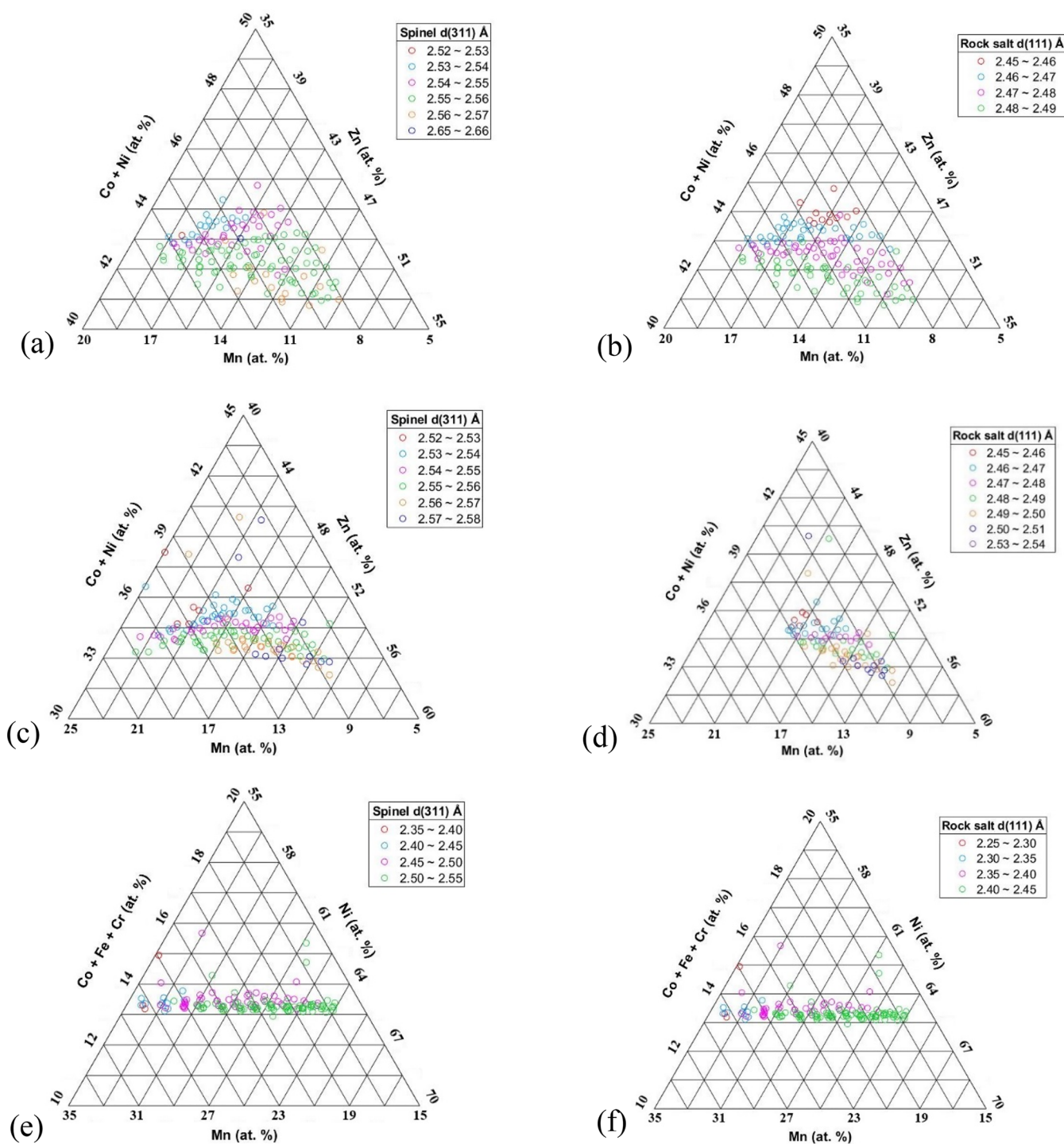
Figure 4. *d*-Spacing of (311) spinel diffraction plane and (111) rock salt diffraction plane of (a and b) RS1, (c and d) RS2, and (e and f) SP.

To further show the correlation between the elemental concentration and the crystalline structure, the major diffraction peaks of $Q \approx 2.45$ (311 plane) and 2.55 Å^{-1} (111 plane) were selected to represent the phase fraction of the spinel and rock salt structures, respectively. Figure 5 shows the ternary phase ratio diagrams of all the samples. The spinel to rock salt phase ratio was determined by the peak intensity ratio and is expressed as SP/(SP+RS) where SP is spinel and RS is rock salt. In the RS1 film, the spinel structure decreases with decreasing Mn and increasing Zn concentrations; while the rock salt structure increases with decreasing Mn and increasing Zn concentrations,

as shown in Figures 5a and S5a. Spinel structure dominates in the Mn-rich region, rock salt domination is in the Zn-rich region. Likewise, the same trends were observed in RS2, as shown in Figure S5b. However, single phase spinel structure was observed on RS2 near the Mn-rich region in the Mn and Zn pseudobinary. The single-phase structure was obtained in where the Mn concentration is more than 12 at. % and Zn less than 44 at. %. The dependence of crystalline structure on the elemental concentration was not observed when Co and Ni were considered due to their insignificant composition spreads. For the SP film, the same structure-concentration dependence was
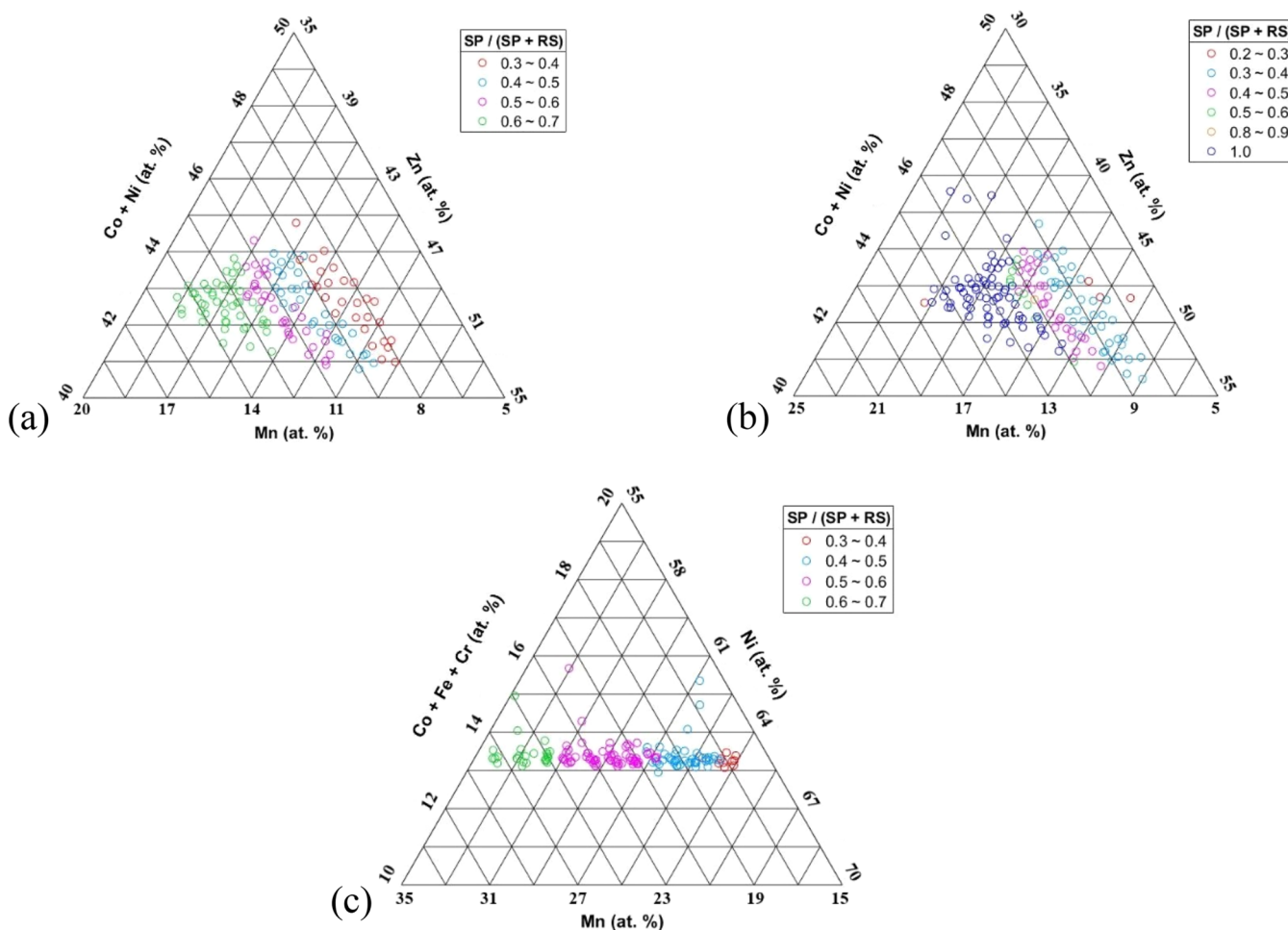
Figure 5. Ternary phase diagrams for phase ratio of (a) RS1, (b) RS2, and (c) SP.

found when considering Mn and Ni, as shown in Figures 5c and S5c. On the other hand, the structure−property relation was investigated by considering the change of sheet resistance with varying grain size. The crystalline grain size was calculated using the Scherrer's equation $t = \frac{k}{B \cos \theta_B}$, where k is shape factor (0.9), λ is the X-ray wavelength (nm), B (radians) is the full width at half-maximum, and θ_B (radians) is the Bragg's angle. The spinel (311) diffraction peak was used to do the calculation. Figure S6 shows the sheet resistance as a function the of crystalline grain size for RS1 and RS2 films. The sheet resistance in general decreases with grain size. As mentioned above, sheet resistance was also found to decrease with increasing Mn concentration for both RS1 and RS2 films. As shown in Figure S5, Mn-rich region exhibits spinel-rich structure. This indicates the film sheet resistance dominates by the spinel phase and decreases with the spinel grain size.

TEM analysis was further used to examine the crystalline structure of RS2. Three spots near the left edge, center, and right edge across the central horizontal line on the wafer were investigated. The HRTEM image and the diffraction pattern shown in Figure 6a indicate single-phase spinel at the left edge. In center region, TEM analysis show the coexistence of spinel and rock salt (Figure 6b). Moving toward to right, rock salt phase dominates with spinel as the minor phase (Figure 6c). The TEM-EDS mappings of the three spots were also examined and are shown in Figure 5d−f, respectively. All the elements distribute homogeneously. The thickness is slightly and

gradually becoming thicker from the Mn rich to Zn-rich region or from the single-phased spinel to the rock salt rich regions. This is attributed to the higher sputtering yield of Zn and the lower density of rock salt phase. The concentrations of elements were also obtained and are listed in Table S1. The data are consistent with the XRF data.

The calculated formation energy, that is, the energy difference between the HEO structure and its constituents at the ground state, using DFT simulation also supports that Mn-poor and Zn- or Ni-rich regions favor the formation of rock salt phase. Figure 7 shows that the formation of rock salt phase is more favorable with reducing Mn concentration. On the other hand, spinel phase is favorable at higher Mn concentrations (Figure S7). Spinel oxide is known to have much higher conductivity than rock salt oxide. As a result, the sheet resistance decreases with the spinel phase (Figure S8). In the single-phase region, the sheet resistance sharply dropped. In other words, the aforementioned continuous decrease of sheet resistance with the Mn concentration along the Mn and Zn pseudobinary in the RS2 film roots in the structural variation.

■ CONCLUSIONS

We have demonstrated the use of a combinatorial sputtering technique to deposit HEO thin films on 76.2 mm wafers. Two type of HEOs were investigated, namely, $(MgZnMnCoNi)O_x$ and $(CrFeMnCoNi)O_x$. The resulting HEO thin films are characterized using several high throughput analytical techni-
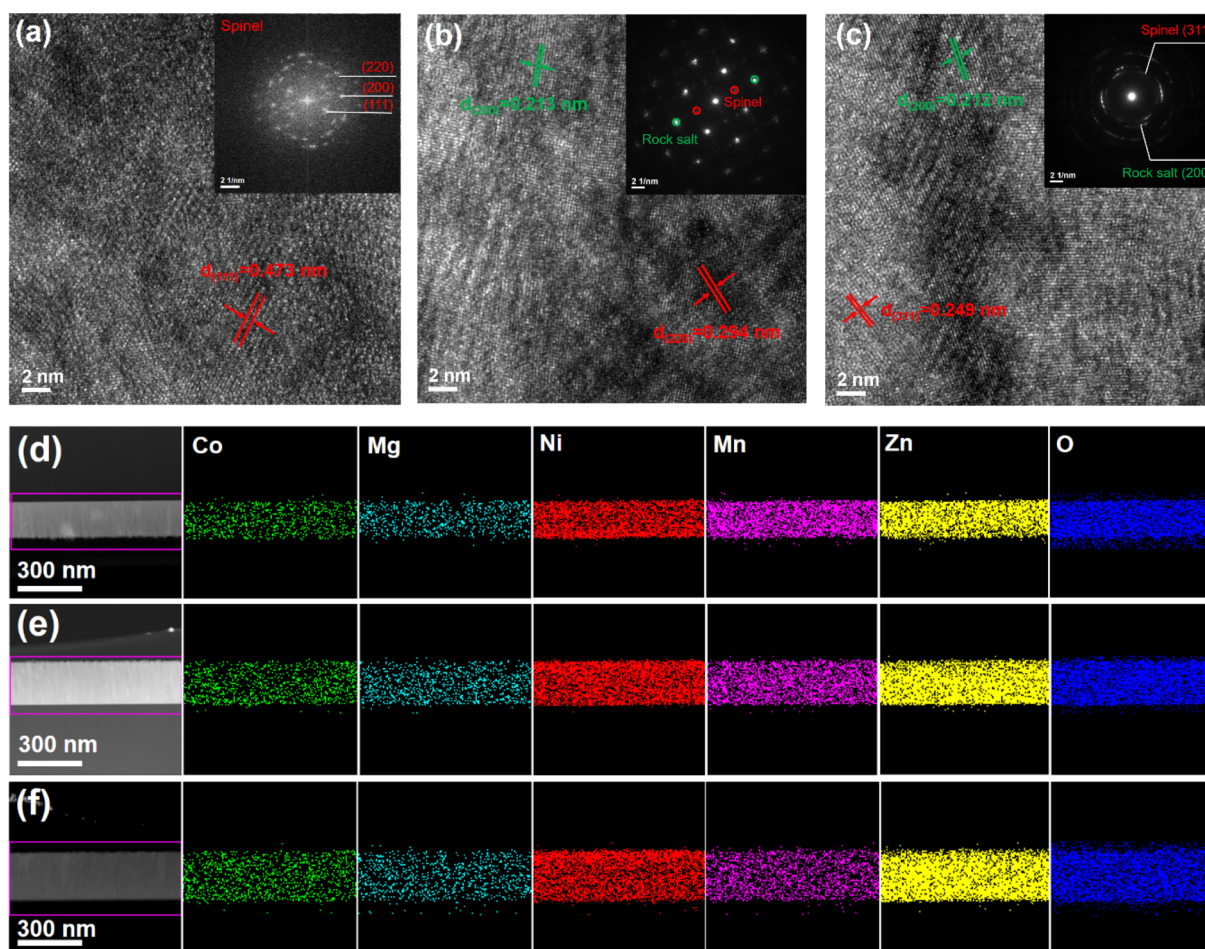
Figure 6. HRTEM and corresponding SEAD of three local positions through the center horizontal line (a) right edge, (b) center, and (c) left edge. TEM-EDS mappings of the above three spots: (d) left edge, (e) center, and (f) right edge.
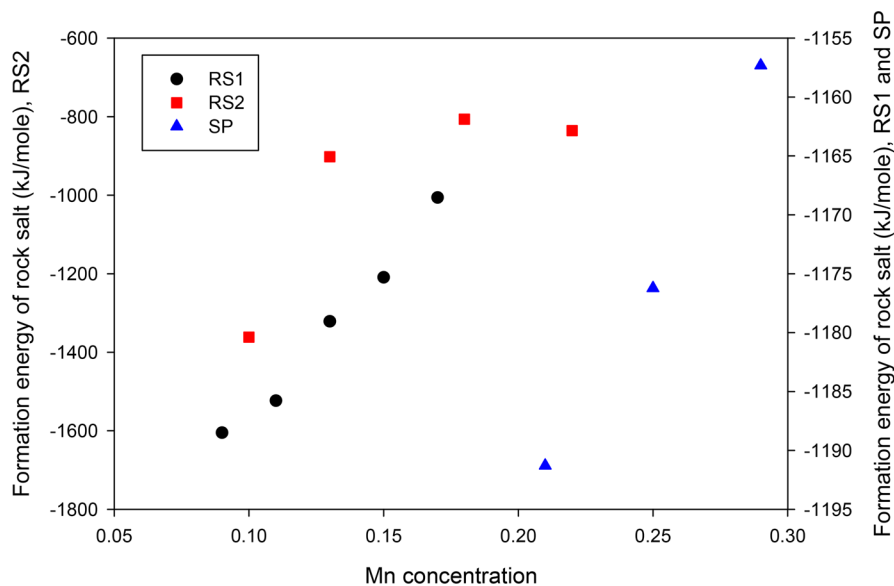
Figure 7. DFT formation enthalpy energy of rock salt phase as a function of Mn concentration.

ques with defined grid maps. Mn and Zn show excellent composition spreads across the $(MgZnMnCoNi)O_x$ films, giving opposite concentration dependence on the grid maps. For the $(CrFeMnCoNi)O_x$ film (SP), Mn and Ni spread across films, also showing opposite concentration dependence on the

grid map. Synchrotron XRD scanning shows that the crystalline phase in the film is composition-controlled. The Mn-rich, Zn-poor region in the $(MgZnMnCoNi)O_x$ film and the Mn-rich, Ni-poor region in the $(CrFeMnCoNi)O_x$ film favors the formation of the spinel phase. This finding is also supported

by the DFT calculation. Moreover, because of the higher conductivity of spinel oxides, the phase spaces high in spinel also show higher conductivity.

■ ASSOCIATED CONTENT

ⓢ Supporting Information

The Supporting Information is available free of charge at https://pubs.acs.org/doi/10.1021/acscombsci.0c00159.

> Concentration table and plots, structural information, electrical resistance, relations among structure/composition/resistance, and simulation results (PDF)

■ AUTHOR INFORMATION

Corresponding Author

Jyh-Ming Ting − *Department of Materials Science and Engineering, National Cheng Kung University, Tainan 70101, Taiwan;* ⓞ orcid.org/0000-0001-9057-0741; Email: jting@ncku.edu.tw

Authors

Thi Xuyen Nguyen − *Department of Materials Science and Engineering, National Cheng Kung University, Tainan 70101, Taiwan*

Yen-Hsun Su − *Department of Materials Science and Engineering, National Cheng Kung University, Tainan 70101, Taiwan*

Jason Hattrick-Simpers − *Materials Measurement Science Division, National Institute of Standards and Technology, Gaithersburg, Maryland 20899, United States*

Howie Joress − *Materials Measurement Science Division, National Institute of Standards and Technology, Gaithersburg, Maryland 20899, United States*

Takahiro Nagata − *Research Center for Functional Materials, National Institute for Materials Science (NIMS), Tsukuba, Ibaraki 305-0044, Japan;* ⓞ orcid.org/0000-0002-8591-2943

Kao-Shuo Chang − *Department of Materials Science and Engineering, National Cheng Kung University, Tainan 70101, Taiwan;* ⓞ orcid.org/0000-0002-2876-9255

Suchismita Sarker − *Stanford Synchrotron Radiation Lightsource, SLAC National Accelerator Laboratory, Menlo Park, California 94025, United States*

Apurva Mehta − *Stanford Synchrotron Radiation Lightsource, SLAC National Accelerator Laboratory, Menlo Park, California 94025, United States;* ⓞ orcid.org/0000-0003-0870-6932

Complete contact information is available at:
https://pubs.acs.org/10.1021/acscombsci.0c00159

Notes

The authors declare no competing financial interest.

■ ACKNOWLEDGMENTS

■ REFERENCES

(1) Yeh, J. W.; Chen, S. K.; Lin, S. J.; Gan, J. Y.; Chin, T. S.; Shun, T. T.; Tsau, C. H.; Chang, S. Y. Nanostructured high-entropy alloys with multiple principal elements: novel alloy design concepts and outcomes. *Adv. Eng. Mater.* **2004**, *6* (5), 299−303.

(2) Cantor, B.; Chang, I.; Knight, P.; Vincent, A. Microstructural development in equiatomic multicomponent alloys. *Mater. Sci. Eng., A* **2004**, *375*, 213−218.

(3) Rost, C. M.; Sachet, E.; Borman, T.; Moballegh, A.; Dickey, E. C.; Hou, D.; Jones, J. L.; Curtarolo, S.; Maria, J.-P. Entropy-stabilized oxides. *Nat. Commun.* **2015**, *6*, 8485.

(4) Sarkar, A.; Loho, C.; Velasco, L.; Thomas, T.; Bhattacharya, S. S.; Hahn, H.; Djenadic, R. Multicomponent equiatomic rare earth oxides with a narrow band gap and associated praseodymium multivalency. *Dalton Trans.* **2017**, *46* (36), 12167−12176.

(5) Sarkar, A.; Djenadic, R.; Usharani, N. J.; Sanghvi, K. P.; Chakravadhanula, V. S.; Gandhi, A. S.; Hahn, H.; Bhattacharya, S. S. Nanocrystalline multicomponent entropy stabilised transition metal oxides. *J. Eur. Ceram. Soc.* **2017**, *37* (2), 747−754.

(6) Sarkar, A.; Djenadic, R.; Wang, D.; Hein, C.; Kautenburger, R.; Clemens, O.; Hahn, H. Rare earth and transition metal based entropy stabilised perovskite type oxides. *J. Eur. Ceram. Soc.* **2018**, *38* (5), 2318−2327.

(7) Jiang, S.; Hu, T.; Gild, J.; Zhou, N.; Nie, J.; Qin, M.; Harrington, T.; Vecchio, K.; Luo, J. A new class of high-entropy perovskite oxides. *Scr. Mater.* **2018**, *142*, 116−120.

(8) Zhou, J.; Zhang, J.; Zhang, F.; Niu, B.; Lei, L.; Wang, W. High-entropy carbide: A novel class of multicomponent ceramics. *Ceram. Int.* **2018**, *44* (17), 22014−22018.

(9) Castle, E.; Csanádi, T.; Grasso, S.; Dusza, J.; Reece, M. Processing and properties of high-entropy ultra-high temperature carbides. *Sci. Rep.* **2018**, *8* (1), 8609.

(10) Sarker, P.; Harrington, T.; Toher, C.; Oses, C.; Samiee, M.; Maria, J.-P.; Brenner, D. W.; Vecchio, K. S.; Curtarolo, S. High-entropy high-hardness metal carbides discovered by entropy descriptors. *Nat. Commun.* **2018**, *9* (1), 4980.

(11) Yan, X.; Constantin, L.; Lu, Y.; Silvain, J. F.; Nastasi, M.; Cui, B. (Hf0. 2Zr0. 2Ta0. 2Nb0. 2Ti0. 2) C high-entropy ceramics with low thermal conductivity. *J. Am. Ceram. Soc.* **2018**, *101* (10), 4486−4491.

(12) Mayrhofer, P. H.; Kirnbauer, A.; Ertelthaler, P.; Koller, C. M. High-entropy ceramic thin films; A case study on transition metal diborides. *Scr. Mater.* **2018**, *149*, 93−97.

(13) Gild, J.; Zhang, Y.; Harrington, T.; Jiang, S.; Hu, T.; Quinn, M. C.; Mellor, W. M.; Zhou, N.; Vecchio, K.; Luo, J. High-entropy metal diborides: a new class of high-entropy materials and a new type of ultrahigh temperature ceramics. *Sci. Rep.* **2016**, *6*, 37946.

(14) Jin, T.; Sang, X.; Unocic, R. R.; Kinch, R. T.; Liu, X.; Hu, J.; Liu, H.; Dai, S. Mechanochemical-assisted synthesis of high-entropy metal nitride via a soft urea strategy. *Adv. Mater.* **2018**, *30* (23), 1707512.

(15) Tsai, C.-W.; Lai, S.-W.; Cheng, K.-H.; Tsai, M.-H.; Davison, A.; Tsau, C.-H.; Yeh, J.-W. Strong amorphization of high-entropy AlBCrSiTi nitride film. *Thin Solid Films* **2012**, *520* (7), 2613−2618.

(16) Gild, J.; Braun, J.; Kaufmann, K.; Marin, E.; Harrington, T.; Hopkins, P.; Vecchio, K.; Luo, J. A high-entropy silicide:(Mo0. 2Nb0. 2Ta0. 2Ti0. 2W0. 2) Si2. *J. Materiomics* **2019**, *5* (3), 337−343.

(17) Qin, Y.; Liu, J.-X.; Li, F.; Wei, X.; Wu, H.; Zhang, G.-J. A high-entropy silicide by reactive spark plasma sintering. *J. Adv. Ceram.* **2019**, *8* (1), 148−152.

(18) Zhang, R.-Z.; Gucci, F.; Zhu, H.; Chen, K.; Reece, M. J. Data-Driven Design of Ecofriendly Thermoelectric High-Entropy Sulfides. *Inorg. Chem.* **2018**, *57* (20), 13027−13033.

(19) Gao, M. C.; Yeh, J.-W.; Liaw, P. K.; Zhang, Y. *High-Entropy Alloys*; Springer International Publishing: Cham, 2016.

(20) Sarkar, A.; Wang, Q.; Schiele, A.; Chellali, M. R.; Bhattacharya, S. S.; Wang, D.; Brezesinski, T.; Hahn, H.; Velasco, L.; Breitung, B. High-Entropy Oxides: Fundamental Aspects and Electrochemical Properties. *Adv. Mater.* **2019**, *31*, 1806236.

(21) Oses, C.; Toher, C.; Curtarolo, S. High-entropy ceramics. *Nat. Rev. Mater.* **2020**, *5*, 295.

(22) Anand, G.; Wynn, A. P.; Handley, C. M.; Freeman, C. L. Phase stability and distortion in high-entropy oxides. *Acta Mater.* **2018**, *146*, 119−125.

(23) Zhang, J.; Yan, J.; Calder, S.; Zheng, Q.; McGuire, M. A.; Abernathy, D. L.; Ren, Y.; Lapidus, S. H.; Page, K.; Zheng, H.; et al. Long-Range Antiferromagnetic Order in a Rocksalt High Entropy Oxide. *Chem. Mater.* **2019**, *31* (10), 3705−3711.

(24) Berardan, D.; Meena, A.; Franger, S.; Herrero, C.; Dragoe, N. Controlled Jahn-Teller distortion in (MgCoNiCuZn) O-based high entropy oxides. *J. Alloys Compd.* **2017**, *704*, 693−700.

(25) Meisenheimer, P.; Kratofil, T.; Heron, J. Giant enhancement of exchange coupling in entropy-stabilized oxide heterostructures. *Sci. Rep.* **2017**, *7* (1), 13344.

(26) Braun, J. L.; Rost, C. M.; Lim, M.; Giri, A.; Olson, D. H.; Kotsonis, G. N.; Stan, G.; Brenner, D. W.; Maria, J. P.; Hopkins, P. E. Charge-induced disorder controls the thermal conductivity of entropy-stabilized oxides. *Adv. Mater.* **2018**, *30* (51), 1805004.

(27) Bérardan, D.; Franger, S.; Dragoe, D.; Meena, A. K.; Dragoe, N. Colossal dielectric constant in high entropy oxides. *Phys. Status Solidi RRL* **2016**, *10* (4), 328−333.

(28) Sarkar, A.; Velasco, L.; Wang, D.; Wang, Q.; Talasila, G.; de Biasi, L.; Kübel, C.; Brezesinski, T.; Bhattacharya, S. S.; Hahn, H.; et al. High entropy oxides for reversible energy storage. *Nat. Commun.* **2018**, *9* (1), 3400.

(29) Chen, H.; Fu, J.; Zhang, P.; Peng, H.; Abney, C. W.; Jie, K.; Liu, X.; Chi, M.; Dai, S. Entropy-stabilized metal oxide solid solutions as CO oxidation catalysts with high-temperature stability. *J. Mater. Chem. A* **2018**, *6* (24), 11129−11133.

(30) Qiu, N.; Chen, H.; Yang, Z.; Sun, S.; Wang, Y.; Cui, Y. A high entropy oxide (Mg0. 2Co0. 2Ni0. 2Cu0. 2Zn0. 2O) with superior lithium storage performance. *J. Alloys Compd.* **2019**, *777*, 767−774.

(31) Nguyen, T. X.; Patra, J.; Chang, J.-K.; Ting, J.-M. High entropy spinel oxide nanoparticles for superior lithiation-delithiation performance. *J. Mater. Chem. A* **2020**, *8* (36), 18963−18973.

(32) Dąbrowa, J.; Stygar, M.; Mikuła, A.; Knapik, A.; Mroczka, K.; Tejchman, W.; Danielewski, M.; Martin, M. Synthesis and micro-structure of the (Co, Cr, Fe, Mn, Ni) 3O4 high entropy oxide characterized by spinel structure. *Mater. Lett.* **2018**, *216*, 32−36.

(33) Grzesik, Z.; Smoła, G.; Miszczak, M.; Stygar, M.; Dąbrowa, J.; Zajusz, M.; Świerczek, K.; Danielewski, M. Defect structure and transport properties of (Co, Cr, Fe, Mn, Ni) 3O4 spinel-structured high entropy oxide. *J. Eur. Ceram. Soc.* **2020**, *40* (3), 835−839.

(34) Mao, A.; Zhang, Z.-G.; Zhang, H.; Ran, S.; et al. A novel six-component spinel-structure high-entropy oxide with ferrimagnetic property. *J. Magn. Magn. Mater.* **2020**, *503*, 166594.

(35) Wang, D.; Liu, Z.; Du, S.; Zhang, Y.; Li, H.; Xiao, Z.; Chen, W.; Chen, R.; Wang, Y.; Zou, Y.; et al. Low-temperature synthesis of small-sized high-entropy oxides for water oxidation. *J. Mater. Chem. A* **2019**, *7* (42), 24211−24216.

(36) Sharma, Y.; Musico, B. L.; Gao, X.; Hua, C.; May, A. F.; Herklotz, A.; Rastogi, A.; Mandrus, D.; Yan, J.; Lee, H. N.; et al. Single-crystal high entropy perovskite oxide epitaxial films. *Phys. Rev. Mater.* **2018**, *2* (6), 060404.

(37) Xiang, X.-D.; Sun, X.; Briceno, G.; Lou, Y.; Wang, K.-A.; Chang, H.; Wallace-Freedman, W. G.; Chen, S.-W.; Schultz, P. G. A combinatorial approach to materials discovery. *Science* **1995**, *268* (5218), 1738−1740.

(38) Koinuma, H.; Takeuchi, I. Combinatorial solid-state chemistry of inorganic materials. *Nat. Mater.* **2004**, *3* (7), 429−438.

(39) Green, M. L.; Takeuchi, I.; Hattrick-Simpers, J. R. Applications of high throughput (combinatorial) methodologies to electronic, magnetic, optical, and energy-related materials. *J. Appl. Phys.* **2013**, *113* (23), 231101.

(40) Shannon, R. D. Revised effective ionic radii and systematic studies of interatomic distances in halides and chalcogenides. *Acta Crystallogr., Sect. A: Cryst. Phys., Diffr., Theor. Gen. Crystallogr.* **1976**, *32* (5), 751−767.

(41) Hume-Rothery, W.; Powell, H. M. On the theory of super-lattice structures in alloys. *Z. Kristallogr. - Cryst. Mater.* **1935**, *91* (1−6), 23−47.

(42) Gregoire, J.; Van Campen, D.; Miller, C.; Jones, R.; Suram, S.; Mehta, A. High-throughput synchrotron X-ray diffraction for combinatorial phase mapping. *J. Synchrotron Radiat.* **2014**, *21* (6), 1262−1268.

(43) Ren, F.; Pandolfi, R.; Van Campen, D.; Hexemer, A.; Mehta, A. On-the-fly data assessment for high-throughput X-ray diffraction measurements. *ACS Comb. Sci.* **2017**, *19* (6), 377−385.

(44) Perdew, J. P.; Burke, K.; Ernzerhof, M. Generalized gradient approximation made simple. *Phys. Rev. Lett.* **1996**, *77* (18), 3865.